Soil moisture and vegetation optical depth retrievals over heterogeneous scenes using LEWIS L-band radiometer

M. Barrée, Arnaud Mialon, Thierry Pellarin, Marie Parrens, Romain Biron, François Lemaître, Simon Gascoin, Yann H. Kerr

Contents lists available at ScienceDirect

International Journal of Applied Earth Observations and Geoinformation

Soil moisture and vegetation optical depth retrievals over heterogeneous scenes using LEWIS L-band radiometer[☆]

M. Barrée [a], A. Mialon [a,*], T. Pellarin [b], M. Parrens [a,c], R. Biron [b], F. Lemaître [d], S. Gascoin [a], Y. H. Kerr [a]

[a] CESBIO, Université de Toulouse, CNES/CNRS/INRAe/IRD/UPS, Toulouse, France
[b] Univ. Grenoble Alpes, CNRS, IRD, Grenoble INP, IGE, Grenoble F-38000, France
[c] Dynafor, Université de Toulouse, INRAE, INPT, INP-PURPAN, Castanet-Tolosan, France
[d] ONERA, Toulouse, France

ABSTRACT

The Soil Moisture and Ocean Salinity (SMOS) satellite has been providing global data for more than 11 years. The algorithm to retrieve surface soil moisture (SM) and vegetation optical depth (VOD) from Brightness Temperatures (TB) has constantly evolved as our understanding of the instrument and of the responses to various ecosystems increased. The evolution of the radiative transfer modelling used in the inversion process is in part based upon ground measurements done on experimental sites. We present the particular case of an L-band radiometer placed on top of a 800- meter-high cliff. This design allows us to study large and various scenes when compared to classical experiments where a radiometer is placed 10–20 m above a surface. With our set up, the footprints cover areas larger than 300 m in diameter, covering thus several land use types and the footprint can be directed towards different dominant land classes (forest, crops, urban etc…). This paper presents the whole set up consisting of in situ measurements (soil moisture and surface temperatures) and L-band radiometry acquired by the LEWIS instrument at high incidence angles. We perform SM/VOD retrievals from brightness temperatures using various configurations which are compared to the in situ observations. We test in particular a 2-VOD retrieval approach that consists in deriving one SM for the entire scene but two VOD, one for agricultural/low vegetation and a VOD for the forest parts, which improves the performance of the SM/VOD retrievals.

1. Introduction

Surface Soil Moisture (SM) is a key variable that controls the interactions between the hydrosphere, the biosphere and the atmosphere, as it drives both soil evaporation and plant transpiration. The importance of soil moisture was showed for climate change (Douville and Chauvin, 2000), surface atmosphere interactions (Koster et al., 2004), weather forecast (Drusch, 2007) and agriculture applications (Chakrabarti et al., 2014).

Remote sensing acquired in the microwave domain, and in particular the lower frequencies, has demonstrated a quantitative ability to measure surface soil moisture under a variety of surface conditions (Jackson, 1993; Njoku and Entekhabi, 1996; Wigneron et al., 2003). The high sensitivity to water of the Brightness Temperature (TB) measurements acquired in the protected microwave range of 1–2 GHz (L-band) make them suitable for surface soil moisture

observations. Recently, two satellite missions were launched for soil moisture observation purposes: (i) the European Space Agency (ESA) / Centre National d'Etudes Spatiales (CNES) 's Soil Moisture Ocean Salinity (SMOS) satellite (Kerr et al., 2001) launched in November 2009 and (ii) the National Aeronautics and Space Administration (NASA) 's Soil Moisture Active and Passive (SMAP) satellite (Entekhabi et al., 2010) launched in January 2015.

SMOS acquires TB at various incidence angles which enables to derive a surface soil moisture and a Vegetation Optical Depth (VOD). The retrieval algorithm is based on the L-band Microwave Emission of the Biosphere (L-MEB) radiative transfer model updated through extensive reviews of state of the art development of the microwave emission of various land cover types (Wigneron et al., 2007; Wigneron et al., 2017; Kerr et al., 2012). Retrieval algorithms were developed and calibrated using data collected over various land conditions from either tower-based experiments (De Rosnay (2015)) with the drawback of

observing small areas (unique land cover), or airborne campaigns (Bircher et al. (2012)) which does not allow long time series of observations.

An experimental site was then specially set up to study heterogeneous areas observed by a radiometer as it is the case for the satellite sensor. This paper presents the "SMOS-Alps" site located in the French Alps where the LEWIS (L-band radiometer for Estimating Water In Soil) radiometer (Lemaître et al., 2004) is installed on the ridge of a cliff to measure the L-band emission of the valley. This set-up enables to use incidence angles higher than 55° that are excluded from SMOS retrieval (Kerr et al., 2012).

This work focuses on the experimental set-up the dataset acquired during the 2015 experiment with the aim of addressing two objectives: (i) consider TB acquired at high incidence angles (ii) evaluate SM-VOD retrievals over heterogeneous scenes. Current SMOS algorithms, i.e. SMOS-IC (Fernandez-Moran et al., 2017) and ESA level 2 (Kerr et al., 2010), are used as well as a special configuration with one derived SM and two derived VOD par scenes.

2. Experimental set-up

2.1. Radiometer experiment

Saint Hilaire du Touvet is located North of Grenoble in the French Alps, where the LEWIS instrument was installed on the ridge of a cliff at an altitude of 1030 m to acquire TB at L-band of different sites down in the flat valley 800 m below. The main specifications of the instrument are reported in Table 1 (Lemaître et al., 2004). The difference in altitude led to large footprints ($\sim$ 200–500 m) which were composed with various landcovers. In order to avoid obstruction by the cliff where it overhung, LEWIS observed the scenes with a relatively high incidence angle (Table 2). Five scenes of interest were selected, referred-to as LAKE, CENTER, FARM, FOREST and CITY (Fig. 1), and were monitored continuously. Each acquisitions were done with a 8 s integration time to maximise sensitivity. Each scene were monitored three consecutive integration time (3 x 8 s) before the instrument moved to the next scenes. An optical camera and a pyrometer were mounted alongside the radiometer to take images of the observed scenes and their skin temperatures (pyrometer KT19.85 9.6 −11.5 m).

This paper focuses on the LAKE, CENTER and FARM scenes. The CITY scene was not studied as no dielectric model was available yet for such scenes. The FOREST scene was located at the bottom of the cliff and presented high topography effects which was also out of the scope of the present study. Fig. 2 presents a sample of TB time series measured in 2015 for the LAKE scene, H and V polarizations as well as the skin temperature measured by the KT19 sensor.

2.2. In situ data

Three sites (Fig. 4) were selected in the valley to collect *in situ* soil moisture and temperature data. At each site, soil moisture were measured at 5 cm, 10 cm, 20 cm, 30 cm and 50 cm soil depths every 15 min. Soil moisture at site 1 were measured with Delta-T devices since April 2, 2014. The sites 2 and 3 were equipped with decagon CS650 probes measuring both soil moisture and soil temperature. The probes were installed on June 16, 2015 at site 2 and on October 8, 2015 at site 3. Site 1 is located close to the Antan farm included in the scene FARM.

Table 1
Lewis radiometer features.

Frequency	Beamwidth	Orientation	Accuracy	Integration time	Calibration
L-band 1.4 GHz	13.6^o	azimuth elevation	< 0.5 K	2s	deep sky TBH = 6.7, TBV = 5.8

Table 2
Scenes features.

Name	Incidence	Information	Footprint, Ellipse dim. (in m.) per axe	Angle (^{o})	semi-minor x semi-major
LAKE	64	Montfort pond, forest	212 × 622		
CENTER	60	forest, cropland	186 × 502		
FARM	66	Antan farm	229 × 695		
FOREST	45	forest	71 × 153		
CITY	67	buildings	168 × 423		

Site 2 was located at a border of an agricultural field and a forest while site 3 was located in a grassland field with a few trees near the Montfort pond (Fig. 4).

Finally, air temperature and rainfall were recorded by a weather station installed at the *in situ* site 1 whereas the soil clay/sand content were measured at each site as reported in Table 3. Fig. 3 presents the SM at a 5-cm depth for each sites along with the rainfall.

2.3. Land cover classification

The land cover classification was derived from the Cartes d'Occupation des SOls (OSO) for 2018 (Inglada et al., 2017). The OSO maps were produced and delivered by the Centre d'Expertise Scientifique sur l'occupation des sols (CES OSO), which is part of Theia national center for data and services on continental surfaces. The maps were provided at a ten-meter spatial resolution and classify the land cover into 23 categories over France. We used the map of 2018 (Fig. 4).

2.4. NDVI

The Normalized Difference Vegetation Index (NDVI) was used to quantify vegetation greenness and was useful for understanding vegetation seasonal evolution. The NDVI was computed as the difference between near-infrared (NIR) and red (R) reflectance divided by their sum as follows:

$$NDVI = \frac{NIR - R}{NIR + R} \qquad (1)$$

The NDVI ranges between −1 and + 1. Higher values refer to active and dense vegetation, whereas lower positive NDVI values are characteristic of stressed or sparse vegetation. It was derived from the Sentinel-2 mission which was launched June, 23 2015. Optical data were provided with a spatial resolution of 10 m and a revisiting time of five days. The NDVI was computed from level 2A data distributed by Theia land data center. The level 2A products were corrected from atmospheric and slope contributions, and were generated using the MAJA algorithm (Hagolle et al., 2015). Cloud and cloud shadow masks were used to exclude non-valid values.

3. Method

Our objectives were to evaluate SM/VOD retrievals from TB acquired by the LEWIS radiometer at high incidence angles and over the scenes named LAKE, CENTER and FARM. To do so, modeled TB were firstly obtained using *in situ* information and the radiative transfer model L-MEB (Section 3.1). Secondly, three SM/VOD retrievals were performed. They were based on minimizing a cost function (Section 3.2) but differed from each other such as: (1) V0 considered the scene as homogeneous, so one SM and one VOD were retrieved; (2) V1 considered the scene as heterogeneous, one SM and two VOD were retrieved (one for forest and one for lower vegetation such as crops, grass, etc) (3) V2 considered the scene as heterogeneous, one SM and one VOD were retrieved for the low
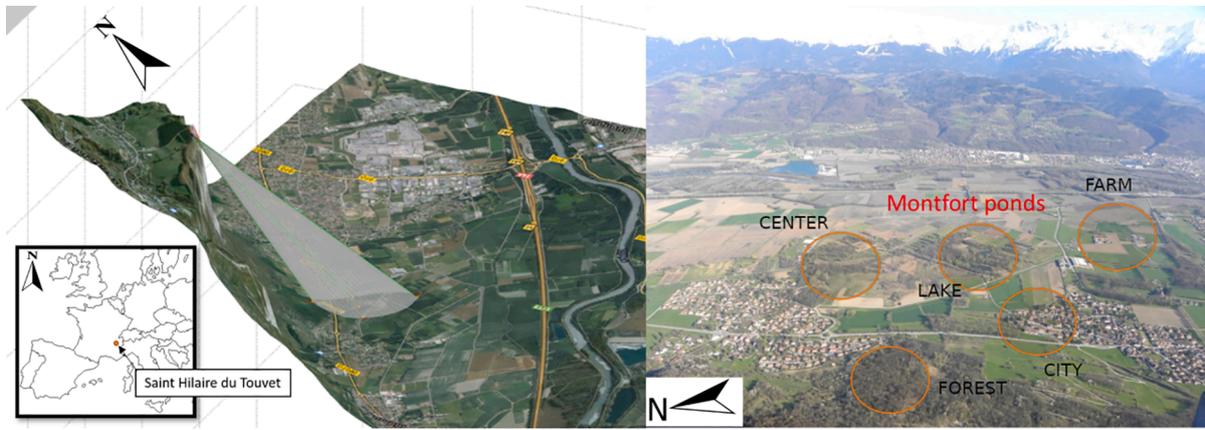
Fig. 1. a) LEWIS location on top of cliff with its field of view in the valley b) The five scenes observed by the instrument.
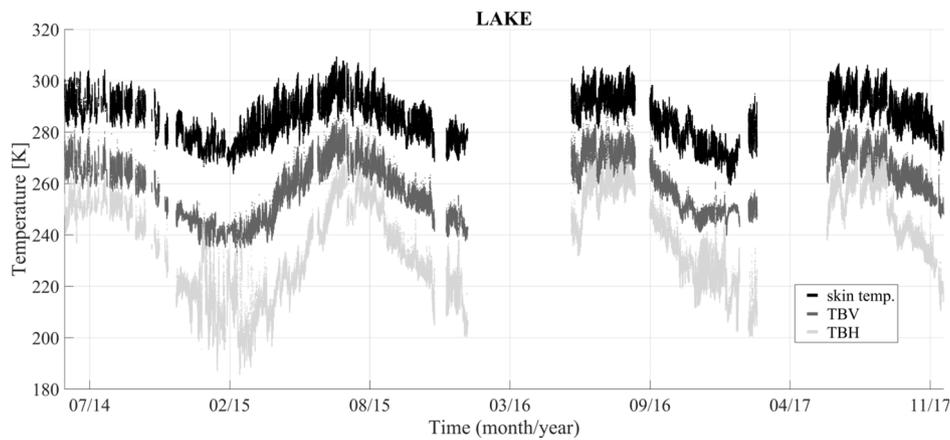

Fig. 2. TB at H and V polarisation measured by LEWIS and the skin temperature sensed by the KT19 probe, in 2014 to 2017.

vegetation land cover, while the VOD for the forest contribution was set to a constant value. V0 was close to the SMOSIC configuration (Fernandez-Moran et al., 2017) while V2 tended to repesent SMOS level 2 (Kerr et al., 2010). V1 was a particular case that was the originality of this work. Finally, the three retrievals (V0, V1, V2) were evaluated using *in situ* surface SM and NDVI for the L-VOD.

3.1. Radiative transfer model

This section presents how the modeled TB were computed using the radiative transfer model L-MEB (Wigneron et al., 2003). The following focuses on the main principles of the L-MEB as it is detailed in Wigneron et al. (2017). The L-MEB represents the soil as a rough surface in contact with a homogeneous vegetation layer, defined by the $\tau - \omega$ model. The TB of the soil/vegetation layer is the sum of (1) the soil emission attenuated by the canopy, (2) the direct vegetation emission and (3) the vegetation emission reflected by the soil and attenuated by the canopy.

$$\text{TB}_p(\theta) = (1 - \omega)(1 - \gamma(\theta)). T_C. \gamma(\theta). r_{G,p}(\theta) + (1 - \omega)(1 - \gamma(\theta)). T_C + (1 - r_{G,p}(\theta)). \gamma(\theta). T_G \quad (2)$$

where T_G and T_C are the effective soil and vegetation temperatures, respectively, r_G is the soil reflectivity, ω is the effective scattering albedo accounting for volume scattering of the canopy and γ is the vegetation attenuation factor; p and θ are the polarization and the incidence angle of the observations.

The soil reflectivity is computed by applying the Fresnel equations (Ulaby, 1982) to the soil permittivity, which is computed with the Mironov model (Mironov et al., 2013). The soil reflectivity is modified to account for surface roughness (Wigneron et al., 2017), which is driven by the parameters H_r and Q_r. In this paper, values of the operational SMOS algorithm are considered such that $H_R = 0.1$ over low vegetation, $H_R = 0.3$ for forest, and $Q_R = 0$, $N_{rV} = 0$, $N_{rH} = 2$ over both low vegetation and forest (Kerr et al., 2012).

The vegetation attenuation factor $\gamma_{(p,\theta)}$ due to the canopy, depends on the angle of incidence and the polarization and is expressed as:

$$\gamma_p(\theta) = \exp(\tau_{nad}/cos\theta) \quad (3)$$

Table 3
Soil composition (sand, silt, clay and organic matters) in percentage for each in situ site.

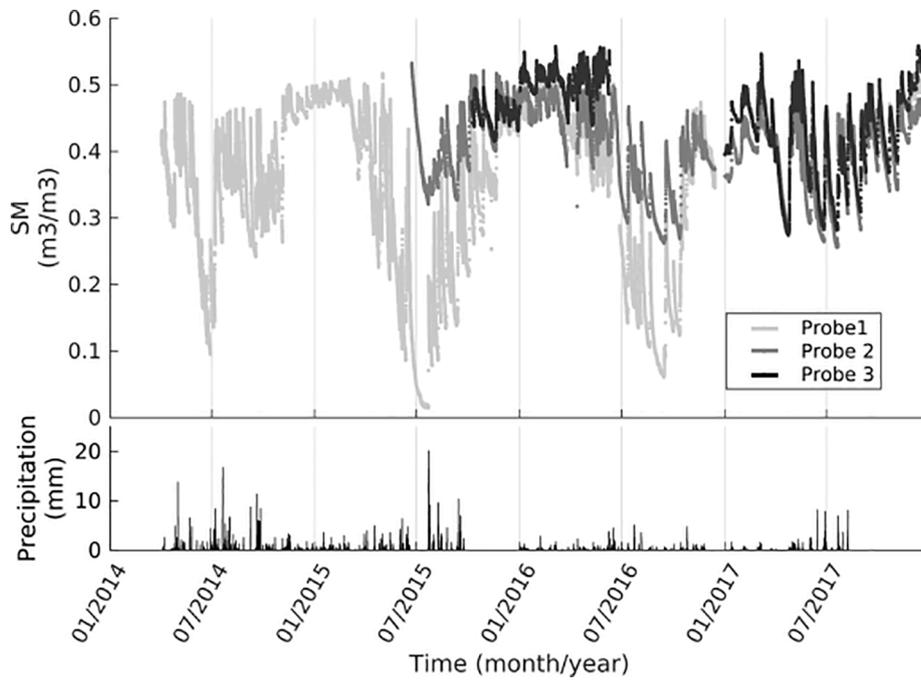| Site	Sand (%)	Silt (%)	Clay (%)	Organic Matters (%)
1	3.1	84.6	12.3	28.5
2	7.8	80	12.2	14.7
3	17	73	10	19.3

Fig. 3. Top) Soil moisture measured at 5 cm depth for the three sites (experiments started in April 2014 for site 1, in June 2015 for site 2 and in October 2015 for site 3); Bottom) precipitation data measured in mm over the site 1 during 2014–2018 period.
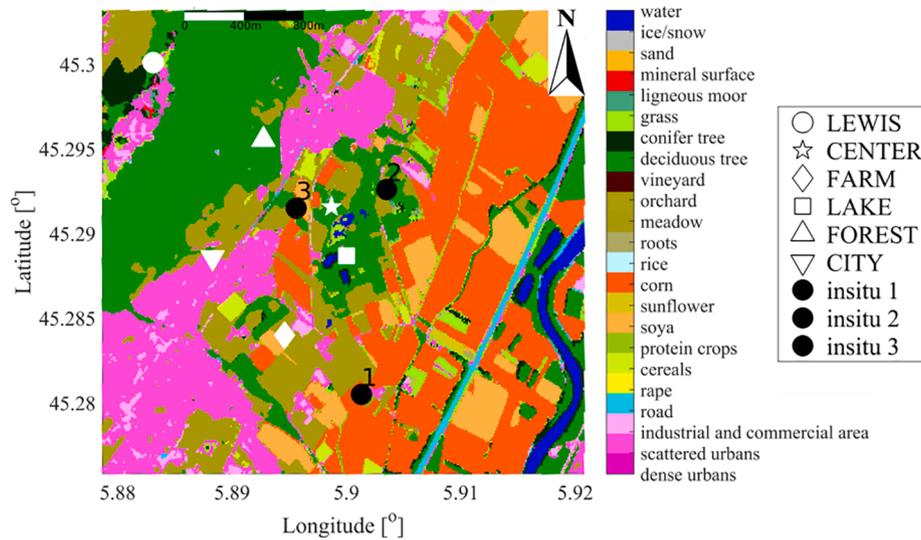

Fig. 4. Land cover map for 2018 in the Valley from the CES OSO (Inglada et al., 2017). White symbols marked the scene locations, the white dots stands for the LEWIS radiometer, whereas the black dots are the *.in situ sites.*

τ_{nad} is the Vegetation Optical Depth (VOD) at nadir and is independent of both the angle of incidence and the polarization. ω_p represents the single scattering albedo with ω_H and ω_V being both set to 0 for low vegetation and to 0.08 for forests (Kerr et al., 2012).

The effective soil temperature T_G is computed with Eq. 4 (Holmes et al., 2006):

$$T_G = T_{SoilDepth} + C_T \cdot (T_{SoilSurf} - T_{SoilDepth}) \qquad (4)$$

where $T_{SoilDepth}$ is the deep soil temperature (50 cm), $T_{SoilSurf}$ the surface temperature (0 to 5 cm) and C_T a parameter dependent on the soil moisture as $(SM/0.3)^{0.3}$. The effective vegetation temperature (T_C) of the forest is considered as approximately equal to the air temperature at

2 meters, measured at the weather station. For low vegetation, T_C is equal to soil temperature ($T_C = T_{soil}$).

3.2. The retrieval process

3.2.1. General approach

This section details the SM and VOD (τ_{nad}) retrievals which were derived from minimizing a cost function (Eq. 5) using a generalized least-squares iterative algorithm.

$\forall t \in [date_{init} : 6h : date_{end}]$,

Table 4
Coefficients used in the cost function.

Parameters	σ^2	Weight	Target value (= initialization)	bounds
				[lower–upper]
			Retrieval v0	
$TB_{(H,V)}$ [K]	0.5	1	TB_{lewis} (H,V)	
SM [m³/m³]	0.1	10	$SM_{measured}$	0–0.6
τ_{nad}				0–1.4
τ_{nad} (variation)	0.1	20	τ_{nad} 6 h to 12 h before	
			Retrieval v1	
$TB_{(H,V)}$ [K]	0.5	1	TB_{lewis} (H,V)	
SM [m³/m³]	0.1	10	$SM_{measured}$	0–0.6
τ_{nad} low vegetation	0.2	10	mean($\tau_{nad,t-1}$, 0.14)	0–0.65
τ_{nad} forest	0.2	10	mean($\tau_{nad,t-1}$, 0.9)	0–1.3
τ_{nad} (variation)	0.1	10	τ_{nad} 6 h to 12 h before	
			Retrieval v2, τ_{nad} forest $= 0.9$	
$TB_{(H,V)}$ [K]	0.5	1	$TB_{lewis(H,V)}$	
SM [m³/m³]	0.1	10	$SM_{measured}$	0–0.6
τ_{nad} low vegetation	0.2	10	mean($\tau_{nad,t-1}$, 0.14)	0–0.65
τ_{nad} (variation)	0.1	10	τ_{nad} 6 h to 12 h before	

$$Costfunction_t = \sum_{P=H,V} \frac{(TB_{lewis,t,P} - TB_{model,t,P})^2}{\sigma_{lewis}^2}$$
$$+ \sum_{i=sm,\tau_{nad}} weight_{param} \times \frac{(Param_{init,t,i} - Param_{model,t,i})^2}{\sigma_{param}^2} \quad (5)$$
$$+ weight_{variation\ \tau_{nad}} \times \frac{(\tau_{nad,t-1} - \tau_{nad,t})^2}{\sigma_{variation\ \tau_{nad}}^2}$$

with TB$_{lewis}$ being the brightness temperatures acquired by the radiometer, TB$_{model}$ the modeled brightness temperatures, σ_{lewis} the radiometric accuracy of the radiometer (Table 4, second column), *weight* is the weight for each free parameters (SM and τ_{nad}, third column Table 4), σ_{param} the accuracy of the free parameters (second column Table 4, for SM and τ_{nad}), $weight_{variation}$ and $\sigma_{variation}$ are the weight and the accuracy of the temporal constraint applied on τ_{nad} (see rows "τ_{nad}(variation)" in Table 4).

The cost function (Eq. 5) was composed of three parts, one relative to the difference of TB (measured minus modeled), one relative to the derive parameters to guide the retrieval, and a last one to insure a slow variation of the VOD from one day to another. The last two terms of the cost function were meant to control the retrieval. They are used in the SMOS algorithms (Kerr et al., 2012) but are even more important here to

Table 5
Land cover percentage for the LAKE, CENTER and FARM scenes, with the antenna pattern weighting function applied.

Land cover Name	LAKE	CENTER	FARM
deciduous tree	35.52	45.60	9.90
meadow	21.52	21.61	40.14
corn	18.74	9.35	13.87
soy	6.78	7.35	8.80
grass	5.4	2.88	1.47
scattered urbans	3.61	5.33	20.03
water	2.58	2.72	0.03
conifer tree	2.03	0.41	0.39
cereals	1.49	2.75	1.75
sunflower	0.97	0.01	0.00
industrial and commercial area	0.72	1.12	3.51
road	0.28	0.24	0.04
ligneous moor	0.19	0.56	0.00
roots	0.17	0.05	0.01
rape	0.00	0.00	0.05

account for the fact that only a unique incidence angle is available. The antenna pattern of the radiometer was taken into account for each scene according to the incidence angle to better reflect the surface monitored by the instrument. Eq. 5 is adapted for each retrievals (V0, V1 and V2) as indicated in Table 4.

3.2.2. Homogeneous retrieval V0

The retrieval V0 considered the observed scene as homogeneous, making the assumption that the whole footprint was covered by a unique landcover class. One set of parameters of the L-MEB model was then defined corresponding to the low vegetation class (Table 5). The target value for τ_{nad} was driven by a lower and an upper value and a strong constraint on its time variation. In average, the CENTER, LAKE and FARM scenes, were defined with an ω equal to 0.036, 0.030 and 0.008, respectively. Similarly, roughness parameter H_r was set to 0.18, 0.17 and 0.12 for the CENTER, LAKE and FARM scene.

3.2.3. Heterogeneous retrievals V1 & V2

The two heterogeneous cases, retrievals V1 and V2, used the OSO map classification to describe the landscape (Fig. 4 and Table 5). The OSO maps were projected onto a 10 m resolution grid and the detailed land classes are grouped into four main classes: low vegetation, forest, urban and water. For a given scene, the total brightness temperature (H, V) was computed as the weighted sum of the brightness temperatures of each pixel as in Eq. 6.

$$TB = \sum_{p=1}^{n_{pixels}} w_p \times TB_p \quad (6)$$

The weight w_p of each pixel was computed using the antenna pattern of LEWIS. Consequently the term TB_P in Eq. 6 were specified as follow:

$$\begin{cases} TB_p = TB_{urban} & \text{if landcover}_{pixel} = \text{urban and built} - \text{up} \\ TB_p = TB_{cropland} & \text{if landcover}_{pixel} = \text{cropland and natural vegetation mosaic} \\ TB_p = TB_{forest} & \text{if landcover}_{pixel} = \text{mixed forest} \\ TB_p = TB_{water} & \text{if landcover}_{pixel} = \text{water} \end{cases}$$

Retrieval V1 considered one SM for the whole scene whereas four τ_{NAD} characterized the four main land surface classes that are low/sparse vegetation, forest, human-made buildings and open water. The τ_{nad} for water and urban were set to 0. Three parameters, i.e. one SM, one VOD of low vegetation, one VOD of forest, were therefore retrieved at the same time using parameters in Table 4.

The last retrieval V2 was similar to V1 in terms of surface heterogeneity. The forest contribution was however fixed and set to 0.9 as observed by SMOS level 2 in average for temporal forests. The retrieval was then done over the low vegetation fraction, so one SM and one VOD were derived in this configuration, which reflected the actual ESA level 2 (Kerr et al., 2012).

4. Results

4.1. LAKE scene

The LAKE scene was characterized by its land surface heterogeneity (37.55% of forest, 55.2% of agricultural fields, 4.7% human-built structures and 2% of open water, Table 5). The derived SM and VOD are presented in Fig. 5 for the three retrieval configurations. Retrieval V1 and V2 are very close (bias of 0.02 and 0.01 m³/m³, Table 6) whereas retrieval V0 overestimates the SM when compared to *in situ* conditions (bias equal to 0.12 m³/m³, Table 6). The constraint on the soil moisture is mandatory and leads to a derived SM that follows the *in situ* profiles. The cropland VOD are similar for all the retrievals (bottom Fig. 5) with an increase from May through out spring and summer to reach a maximum by the end of August. From then on, the VOD decreases. Retrievals V1 and V2 show more dynamic and variability than V0.
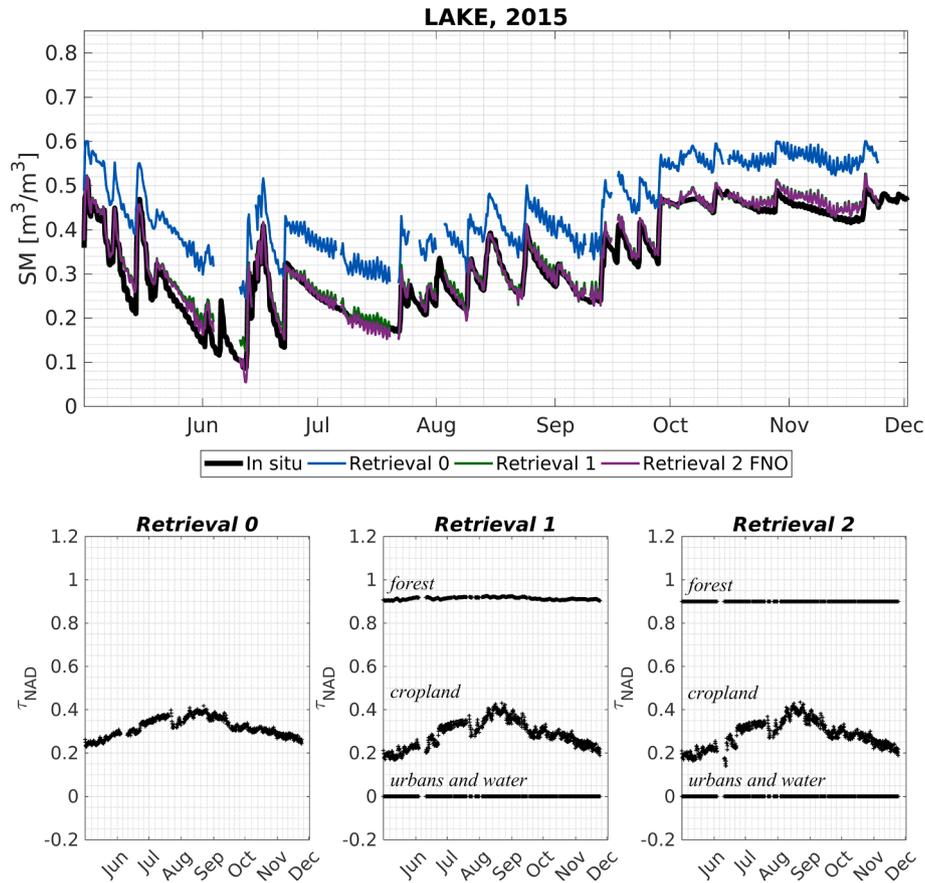
L-band radiometer by a cliff

Fig. 5. Derived SM (top) and VOD (bottom) for retrievals V0, V1 and V2 over the LAKE scene.

Table 6

Statistics for the LAKE, CENTER and FARM scenes. The upper part of the Table is a comparison in terms of TB (K), the lower part in SM (m^3/m^3) as retrieved SM - *in situ*. The number of point is 758. The Pearson correlation coefficients R are in all cases higher than 0.92 and so are not reported in the table.

	LAKE		CENTER		FARM	
Model - Polarization	RMSE	Bias	RMSE	Bias	RMSE	Bias
Retrieval 0 - H	2.04	−1.93	1.87	−1.73	2.76	−2.59
Retrieval 0 - V	11.5	11.38	8.84	8.69	16.36	16.20
Retrieval 1 - H	1.53	−1.32	2.22	−1.76	0.85	−0.67
Retrieval 1 - V	3.12	2.77	2.20	−1.37	3.76	−2.88
Retrieval 2 - H	1.54	−1.33	2.60	−1.97	3.59	−2.51
Retrieval 2 - V	3.41	3.02	2.80	−2.27	14.91	−13.96
SM v0 - *in situ*	0.12	0.12	0.09	0.09	0.17	0.16
SM v1 - *in situ*	0.02	0.02	0.06	−0.05	0.18	−0.16
SM v2 - *in situ*	0.02	0.01	0.04	−0.03	0.07	−0.06

Interesting is the retrieval V1 on the forest fraction for which the VOD shows an almost constant value with a slight seasonal dynamic. The hypothesis of a fixed VOD for the forest contribution, as such set in retrieval V2, seems justified for the case of this particular forest.

The derived SM and VOD (Fig. 5) are also used to compute TB and so to evaluate the performance of the approach at the radiometer level (Table 6). The worst score is obtained for V0 at H polarisation (RMSE of 11.5 K, bias of 11.4 K) suggesting that the configuration of an homogeneous scene is not appropriate in our present case. Retrievals V1 and V2 both perform very well with retrieval V1 showing slightly better performances than retrieval V2 (Table 6).

4.2. CENTER scene

The derived SM over the CENTER site (Fig. 6) shows similar behavior to that of the LAKE scene with retrievals V1 and V2 having a slightly negative bias of −0.05 m^3/m^3 and −0.03 m^3/m^3 (Table 6). Retrieval V0 overestimates the SM compared to *in situ* measurements (0.09 m^3/m^3) but the three derived SM have high correlation coefficients (higher than 0.99).

The VOD values evolve between 0.2 and 0.5 (bottom Fig. 6) with retrieval V1 and V2 having similar patterns. A maximum is observed in late August for the three retrievals but stable conditions are observed in July for retrievals V1 and V2 (croplands) which is not the case for retrieval V0 nor for the LAKE scene. The forest contribution (only derived for retrieval V1) is consistent with the one derived for the TB measured for the LAKE scene. It presents a reduced dynamic around a value of 0.9, with a maximum detected in late August, as for the cropland.

4.3. FARM scene

The FARM scene (Fig. 7) depicts more differences than the two other sites. The derived SM shows a wider range of values with retrieval V0 reaching 0.6 m^3/m^3. This retrieval largely overestimates SM measured at the site except for July where V0 gives low values, which does not occur for retrievals V1 and V2. The causes were identified and are discussed in the next section. On the opposite, V1 SM values are too low (negative bias of 0.16 m^3/m^3, Table 6) and present a reduced dynamics when compared to *in situ* measurements (black line). As for the two other
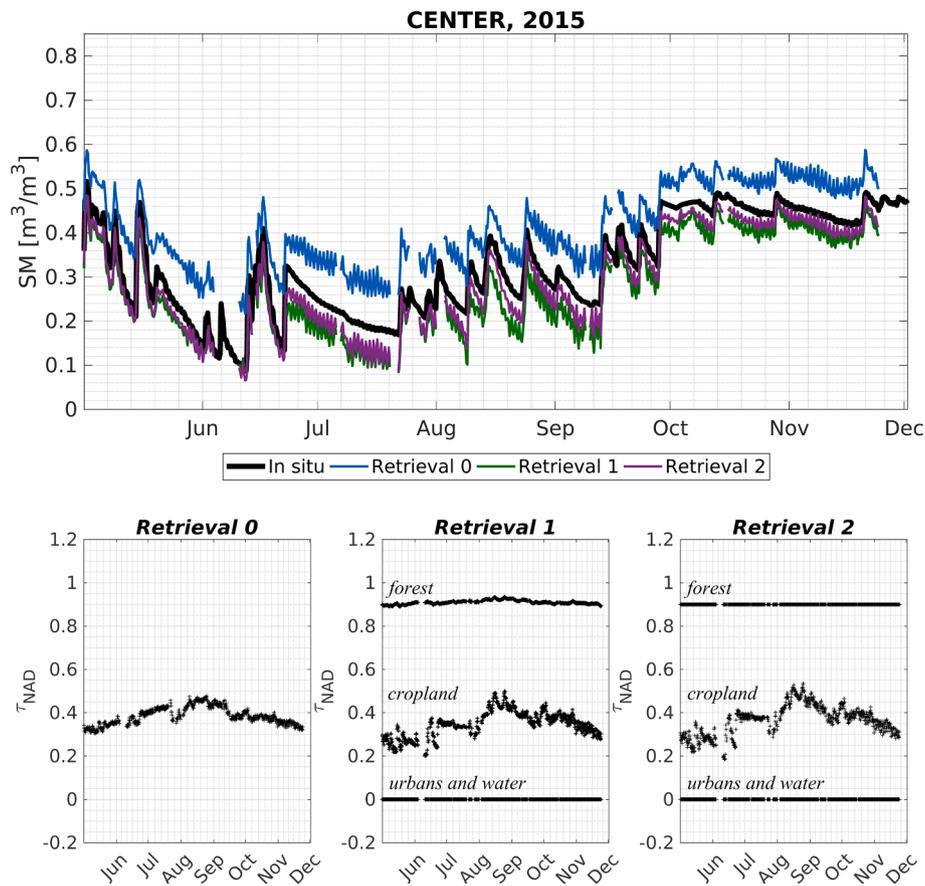
L-band radiometer by a cliff

Fig. 6. Derived SM (top) and VOD (bottom) for retrievals V0, V1 and V2 over the CENTER scene.

sites, V2 retrieval leads to the best SM estimation, with a bias equal to -0.06 m³/m³ compared to *in situ*.

5. Discussion and Conclusion

Various retrieval configurations were tested, among which deriving only SM in a first run and then the VOD in a second run, that is not considered in this article. Only those configurations using a 2-parameter SM-VOD retrieval, with a constraint on the VOD based on previous retrievals were found to be relevant and discussed here. It was found that a temporal constraint is to be set on the VOD in the cost function (Eq. 5) to compensate for the unique incidence angle. Nevertheless, the retrieved SM are well correlated to the *in situ* measurements (correlation coefficients higher than 0.9). The best results are obtained for the LAKE site, which is interesting in terms of surface heterogeneity. Generally, the retrieval V0 considering homogeneous scene overestimates the SM, but still having a high correlation (higher than 0.92) with the *in situ* soil moisture. The retrievals V1 and V2 (heterogeneous landcover) lead to similar results except for the FARM site. Almost ∼ 24% of the footprint (Table 5) of this site is covered by man made structures (houses, buildings, roads) which is significant, especially when compared to the other sites (4.6% for LAKE, 6.5% for CENTER Table 5). The derived SM tends to compensate for the lack of a model for these complex structures and presents a bias which is the highest for the FARM scene (Table 6). That is particularly the case during drying events, which often leads to SM/VOD retrieval failures or very low SM values (Fig. 6 for the month of July). Retrieval V1 is the less impacted as the VOD of croplands compensates by decreasing its values. Actually, the V0 and V1 VOD are lower than V2 (lower panel in Fig. 7), whereas the V0, V1 and V2 are, for

croplands, within the same ranges as for the other sites (Fig. 5 and 6). Tests were undertaken (not shown) and the solution to avoid any V0 retrieval failure was to set the initial SM conditions to very high values (0.4 m³/m³). This leads however to a significant overestimation of SM without seasonal dynamic.

The derived VOD for the decidous forest (Fig. 5 and 6) are almost constant during the year which is expected as the L-VOD is more sensitive to the above ground biomass than to the leaves for temporal decidous forest (Guglielmetti et al., 2007). Nevertheless, the derived VOD for low vegetation and crops presents a seasonal dynamic. As the three cases of study (Fig. 5–7) are similar, the following discussion focuses on the lake scene. The three derived VOD (V0, V1 and V2) are compared to the NDVI (Fig. 8) for which all available years are overlaid to show the seasonal dynamic of the vegetation. The VOD V1 and V2 are close, whereas V0 depicts higher values. The three VOD present a common trend that is an increase in late spring, with a maximum occurring at the end of August - beginning of September followed by a slow decrease, as also observed for crop lands by Patton and Hornbuckle (2012),Wigneron et al. (2012), Lewis-Beck et al. (2020). The NDVI presents low values in winter, an increase in April/May whereas summer is characterized by a constant value and is then followed by a decrease from mid September. The two vegetation proxy are delayed which is in accordance with Wigneron et al. (2012),Chaparro et al. (2018) and Togliatti et al. (2019). The NDVI and VOD also reach their maximum at a different time during the season, the NDVI preceding the L-VOD (as observed by Wang et al. (2020)). It is explained by the fact that the two indices do not measure the same aspect of the vegetation layer, i.e. greenness for the NDVI (related to Chlorophyll activities) whereas the VOD is related to dry vegetation and its vegetation water content
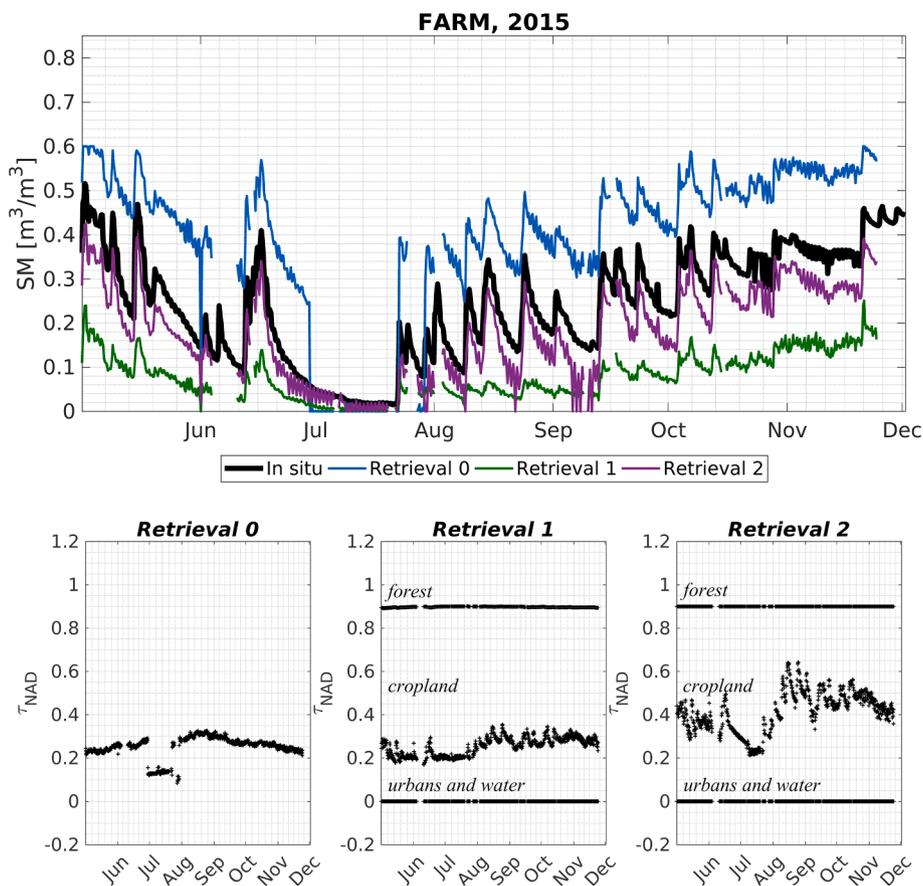
L-band radiometer by a cliff

Fig. 7. Derived SM (top) and VOD (bottom) for retrievals V0, V1 and V2 over the FARM scene.
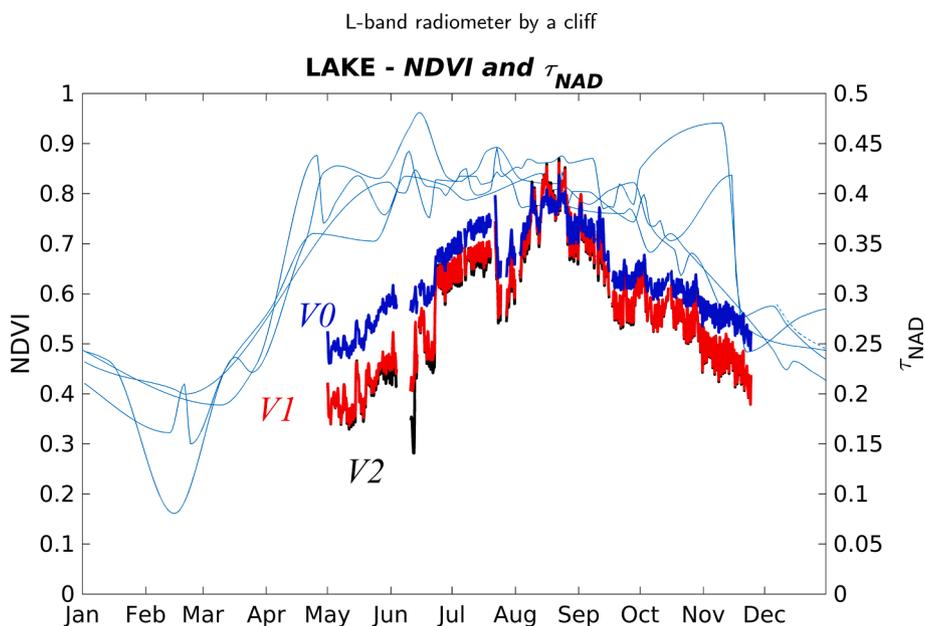
L-band radiometer by a cliff

Fig. 8. Comparison between the τ_{nad} retrieved for V0 (blue line), V1 (red line) and V2 (black line) during 2015 and the NDVI data from Sentinel during the 2015–2019 (light blue lines) over the scene LAKE. (For interpretation of the references to colour in this figure legend, the reader is referred to the web version of this article.)

(Togliatti et al., 2019) which are present after the vegetation is mature.

This study presents the particular experimental set up that proposes an L-band radiometer placed on top of a cliff, overhanging a flat valley.

Compared to existing tower-based experiments, this configuration allow us to observe scenes that are hundred-meter wide and so heterogeneous, with contributions from various surface classes (agricultural fields,

urban areas, ponds and forests), such as what is observed by the SMOS and SMAP satellite missions. Three retrieval approaches were tested to derive surface soil moisture and VOD. Our results suggest that it is of interest to consider the VOD of forest and of lower vegetation separately at L-band. Finally, this database will be used to particularly evaluate the impact of urban and human-made areas.

Declaration of Competing Interest

The authors declare that they have no known competing financial interests or personal relationships that could have appeared to influence the work reported in this paper.

Acknowledgments

References

Bircher, S., Balling, J.E., Skou, N., Kerr, Y.H., 2012. Validation of smos brightness temperatures during the hobe airborne campaign, western Denmark. IEEE Trans. Geosci. Remote Sens. 50, 1468–1482. https://doi.org/10.1109/TGRS.2011.2170177.

Chakrabarti, S., Bongiovanni, T., Judge, J., Zotarelli, L., Bayer, C., 2014. Assimilation of smos soil moisture for quantifying drought impacts on crop yield in agricultural regions. IEEE Journal of Selected Topics in Applied Earth Observations and Remote Sensing 7, 3867–3879.

Chaparro, D., Piles, M., Vall-Llossera, M., Camps, A., Konings, A.G., Entekhabi, D., 2018. L-band vegetation optical depth seasonal metrics for crop yield assessment. Remote Sens. Environ. 212, 249–259. https://doi.org/10.1016/j.rse.2018.04.049.

de Rosnay, P., Calvet, J.-C., Kerr, Y., Wigneron, J.-P., Lemaître, F., Escorihuela, M.J., Muñoz Sabater, J., Saleh, K., Barrié, J., Bouhours, G., Coret, L., Cherel, G., Dedieu, G., Fritz, N.E.D., Froissard, F., Hoedjes, J., Kruszewski, A., Lavenu, F., Suquia, D., Waldteufel, P., 2006. SMOSREX: A long term field campaign experiment for soil moisture and land surface processes remote sensing. Remote Sens. Environ. 102 (3–4), 377–389. https://doi.org/10.1016/j.rse.2006.02.021.

Douville, H., Chauvin, F., 2000. Relevance of soil moisture for seasonal climate predictions: A preliminary study. Clim. Dyn. 16, 719–736.

Drusch, M., 2007. Initializing numerical weather prediction models with satellite-derived surface soil moisture: Data assimilation experiments with ecmwf's integrated forecast system and the tmi soil moisture data set. Journal of Geophysical Research: Atmospheres 112.

Entekhabi, D., Njoku, E.G., O'Neill, P.E., Kellogg, K.H., Crow, W.T., Edelstein, W.N., Entin, J.K., Goodman, S.D.,, T.J., Johnson, J., et al., 2010. The soil moisture active passive (smap) mission. Proceedings of the IEEE 98, 704–716.

Fernandez-Moran, R., Al-Yaari, A., Mialon, A., Mahmoodi, A., Al Bitar, A., De Lannoy, G., Rodriguez-Fernandez, N., Lopez-Baeza, E., Kerr, Y., Wigneron, J.P., 2017. Smos-ic: An alternative smos soil moisture and vegetation optical depth product. Remote Sensing 9. URL: http://www.mdpi.com/2072-4292/9/5/457, doi:10.3390/rs9050457. article Number 457.

Fernández-Morán, R., Wigneron, J.P., Lopez-Baeza, E., Al-Yaari, A., Coll-Pajaron, A., Mialon, A., Miernecki, M., Parrens, M., Salgado-Hernanz, P.M., Schwank, M., et al., 2015. Roughness and vegetation parameterizations at l-band for soil moisture retrievals over a vineyard field. Remote Sens. Environ. 170, 269–279.

Guglielmetti, M., Schwank, M., Mätzler, C., Oberdörster, C., Vanderborght, J., Flühler, H., 2007. Measured microwave radiative transfer properties of a deciduous forest canopy. Remote sensing of environment 109, 523–532.

Hagolle, O., Huc, M., Villa Pascual, D., Dedieu, G., 2015. A multi-temporal and multi-spectral method to estimate aerosol optical thickness over land, for the atmospheric correction of formosat-2, landsat, venµs and sentinel-2 images. Remote Sensing 7, 2668–2691.

Holmes, T.R.H., de Rosnay, P., de Jeu, R., Wigneron, J.P., Kerr, Y.H., Calvet, J.C., Escorihuela, M.J., Saleh, K., Lemaître, F., 2006. A new parameterization of the effective temperature for l band radiometry. Geophys. Res. Let. 33 https://doi.org/10.1029/2006GL025724.

Inglada, J., Vincent, A., Arias, M., Tardy, B., Morin, D., Rodes, I., 2017. Operational high resolution land cover map production at the country scale using satellite image time series. Remote Sensing 9, 95.

Jackson, T.J., 1993. Iii. measuring surface soil moisture using passive microwave remote sensing. Hydrological processes 7, 139–152.

Kerr, Y.H., Waldteufel, P., Richaume, P., Wigneron, J.P., Ferrazzoli, P., Mahmoodi, A., Al Bitar, A., Cabot, F., Gruhier, C., Juglea, S.E., Leroux, D., Mialon, A., Delwart, S., 2012. The SMOS Soil Moisture Retrieval Algorithm. Geoscience and Remote Sensing, IEEE Transactions on 50, 1384–1403. https://doi.org/10.1109/TGRS.2012.2184548.

Kerr, Y.H., Waldteufel, P., Wigneron, J.P., Delwart, S., Cabot, F., Boutin, J., Escorihuela, M.J., Font, J., Reul, N., Gruhier, C., et al., 2010. The smos mission: New tool for monitoring key elements ofthe global water cycle. Proc. IEEE 98, 666–687.

Kerr, Y.H., Waldteufel, P., Wigneron, J.P., Martinuzzi, J., Font, J., Berger, M., 2001. Soil moisture retrieval from space: The soil moisture and ocean salinity (smos) mission. IEEE transactions on Geoscience and remote sensing 39, 1729–1735.

Koster, R.D., Dirmeyer, P.A., Guo, Z., Bonan, G., Chan, E., Cox, P., Gordon, C., Kanae, S., Kowalczyk, E., Lawrence, D., et al., 2004. Regions of strong coupling between soil moisture and precipitation. Science 305, 1138–1140.

Lemaître, F., Poussiere, J.C., Kerr, Y.H., Déjus, M., Durbe, R., de Rosnay, P., Calvet, J.C., 2004. Design and test of the ground-based l-band radiometer for estimating water in soils (lewis). IEEE Trans. Geosci. Remote Sens. 42, 1666–1676.

Lewis-Beck, C., Walker, V.A., Niemi, J., Caragea, P., Hornbuckle, B.K., 2020. Extracting agronomic information from smos vegetation optical depth in the us corn belt using a nonlinear hierarchical model. Remote Sensing 12, 827.

Mironov, V., Kerr, Y., Wigneron, J.P., Kosolapova, L., Demontoux, F., 2013. Temperature-and texture-dependent dielectric model for moist soils at 1.4 ghz. Geoscience and Remote Sensing Letters, IEEE 10, 419–423.

Njoku, E.G., Entekhabi, D., 1996. Passive microwave remote sensing of soil moisture. Journal of hydrology 184, 101–129.

Patton, J., Hornbuckle, B., 2012. Initial validation of smos vegetation optical thickness in iowa. IEEE Geosci. Remote Sens. Lett. 10, 647–651.

Togliatti, K., Hartman, T., Walker, V.A., Arkebauer, T.J., Suyker, A.E., VanLoocke, A., Hornbuckle, B.K., 2019. Satellite l–band vegetation optical depth is directly proportional to crop water in the us corn belt. Remote Sens. Environ. 233, 111378.

Ulaby, F.T., 1982. Microwave Remote Sensing: Active and Passive, Radar Remote Sensing and Surface Scattering and Emission Theory, volume 2. Addison-Wesley, Reading, Mass.

Wang, X., Dannenberg, M.P., Yan, D., Jones, M.O., Kimball, J.S., Moore, D.J., van Leeuwen, W.J., Didan, K., Smith, W.K., 2020. Globally consistent patterns of asynchrony in vegetation phenology derived from optical, microwave, and fluorescence satellite data. Journal of Geophysical Research: Biogeosciences 125 e2020JG005732.

Wigneron, J., Schwank, M., Lopez Baeza, E., Kerr, Y., Novello, N., Millan, C., Moisy, C., Richaume, P., Mialon, A., Al Bitar, A., Cabot, F., Lawrence, H., Guyon, D., Calvet, J. C., Grant, J.P., Casal, T., de Rosnay, P., Saleh, K., Mahmoodi, A., Delwart, S., Mecklenburg, S., 2012. First evaluation of the simultaneous smos and elbara-ii observations in the mediterranean region. Remote Sens. Environ. 124, 26–37. URL: http://www.sciencedirect.com/science/article/pii/S0034425712001836, doi: https://doi.org/10.1016/j.rse.2012.04.014.

Wigneron, J.P.,, T., O'neill, P., De Lannoy, G., De Rosnay, P., Walker, J., Ferrazzoli, P., Mironov, V., Bircher, S., Grant, J., et al., 2017. Modelling the passive microwave signature from land surfaces: A review of recent results and application to the l-band smos & smap soil moisture retrieval algorithms. Remote Sensing of Environment 192, 238–262.

Wigneron, J.P., Calvet, J.C., Pellarin, T., Van de Griend, A.A., Berger, M., Ferrazzoli, P., 2003. Retrieving near-surface soil moisture from microwave radiometric observations: current status and future plans. Remote Sens. Environ. 85, 489–506.

Wigneron, J.P., Kerr, Y., Waldteufel, P., Saleh, K., Escorihuela, M.J., Richaume, P., Ferrazzoli, P., De Rosnay, P., Gurney, R., Calvet, J.C., et al., 2007. L-band microwave emission of the biosphere (l-meb) model: Description and calibration against experimental data sets over crop fields. Remote Sens. Environ. 107, 639–655.